Frequency split metal artifact reduction (FSMAR) in computed tomography

Esther Meyer
Institute of Medical Physics, University of Erlangen–Nürnberg, 91052 Erlangen, Germany

Rainer Raupach
Siemens Healthcare Forchheim, 91301 Forchheim, Germany

Michael Lell
Institute of Diagnostic Radiology, University of Erlangen–Nürnberg, 91054 Erlangen, Germany

Bernhard Schmidt
Siemens Healthcare Forchheim, 91301 Forchheim, Germany

Marc Kachelrieß[a)]
Institute of Medical Physics, Friedrich-Alexander-University (FAU), 91052 Erlangen, Germany and Medical Physics in Radiology, German Cancer Research Center (DKFZ), 69120 Heidelberg, Germany

Purpose: The problem of metal artifact reduction (MAR) is almost as old as the clinical use of computed tomography itself. When metal implants are present in the field of measurement, severe artifacts degrade the image quality and the diagnostic value of CT images. Up to now, no generally accepted solution to this issue has been found. In this work, a method based on a new MAR concept is presented: frequency split metal artifact reduction (FSMAR). It ensures efficient reduction of metal artifacts at high image quality with enhanced preservation of details close to metal implants.
Methods: FSMAR combines a raw data inpainting-based MAR method with an image-based frequency split approach. Many typical methods for metal artifact reduction are inpainting-based MAR methods and simply replace unreliable parts of the projection data, for example, by linear interpolation. Frequency split approaches were used in CT, for example, by combining two reconstruction methods in order to reduce cone-beam artifacts. FSMAR combines the high frequencies of an uncorrected image, where all available data were used for the reconstruction with the more reliable low frequencies of an image which was corrected with an inpainting-based MAR method. The algorithm is tested in combination with normalized metal artifact reduction (NMAR) and with a standard inpainting-based MAR approach. NMAR is a more sophisticated inpainting-based MAR method, which introduces less new artifacts which may result from interpolation errors. A quantitative evaluation was performed using the examples of a simulation of the XCAT phantom and a scan of a spine phantom. Further evaluation includes patients with different types of metal implants: hip prostheses, dental fillings, neurocoil, and spine fixation, which were scanned with a modern clinical dual source CT scanner.
Results: FSMAR ensures sharp edges and a preservation of anatomical details which is in many cases better than after applying an inpainting-based MAR method only. In contrast to other MAR methods, FSMAR yields images without the usual blurring close to implants.
Conclusions: FSMAR should be used together with NMAR, a combination which ensures an accurate correction of both high and low frequencies. The algorithm is computationally inexpensive compared to iterative methods and methods with complex inpainting schemes. No parameters were chosen manually; it is ready for an application in clinical routine. © *2012 American Association of Physicists in Medicine*. [http://dx.doi.org/10.1118/1.3691902]

Key words: metal artifacts, metal artifact reduction, metal implants

I. INTRODUCTION

I.A. Metal artifact reduction

Metal implants are a major source of artifacts in clinical computed tomography and there is a substantial quantity of publications on metal artifact reduction (MAR). While there are quite different approaches, which vary in complexity of the algorithm and in computational load, they have often one thing in common: those parts of the raw data which are cor-rupted due to metal are replaced or used with a lower weight. This loss of information leads to blurring close to the metal implants. There is still no MAR method which is considered as a generally acceptable solution to this problem.

Metal artifacts include artifacts due to noise, beam hard-ening, scatter, and nonlinear partial volume effect and they often have magnitudes of several hundred Hounsfield units. Due to the high densities and atomic numbers of metal, those effects are much more severe for cases with metal in the field

of measurement than for cases without metal. The term *metal artifacts* is generic and describes the artifacts resulting from all these effects. Metal artifacts in CT images appear as fine streak artifacts and broader dark or bright band artifacts due to beam hardening and scatter. While the streak artifacts due to noise surely reduce the image quality, the band artifacts often obscure areas close to metal completely, and they can drastically reduce the diagnostic value of images. In Fig. 1, four examples are shown. The first example (counted from left to right) is a patient with a bilateral hip endoprosthesis. Artifacts are strongest in the area between the two implants. The second example is a patient after coiling of an intracranial aneurysm. The third example is a patient with a fixation of the spine. Two rods are placed in parallel to the spinal column and screws into the vertebrae hold it together. The fourth example in Fig. 1 is a patient with several dental fillings, which is a very common case. Dental fillings and crowns are often very dense and irregular shaped and especially when a patient has multiple metal parts within one slice, artifacts are particularly strong.

To reduce metal artifacts, one can either replace corrupted raw data or try to really correct them. Because replacing data and the consequential loss of data lead to blurring, a physical correction seems to be a desirable goal at first. Excessive noise, for example, can be reduced by adaptive filtering.[1] However, in many cases, it is a very difficult task to physically correct the beam hardening and scatter parts of metal artifacts. The success of a physical correction heavily depends on the type of metal implant. To the authors, inpainting-based MAR methods seem to be a more robust solution so far.

The term inpainting refers to an algorithm for replacing parts of an image. Inpainting-based methods for MAR consider those parts of the projection data that are affected by metal (the so-called metal trace or metal shadow) as completely unreliable. Different interpolation methods, for example, in Refs. 2–8 or more general inpainting approaches, can be used to replace these data. Examples of inpainting-based MAR methods using forward projections to fill the gaps from the metal shadow can be found in Refs. 7 and 9–15. Methods of this type are comparatively robust, but the assumption that the data from the metal trace are completely useless is only valid for very thick and dense implants where photon starvation sets in. The region close to metal implants is often not well corrected when inpainting-based MAR methods are used, especially if the metal implants do not have circular cross-sections. More details are found in Sec. II B 3.

Other MAR methods use additional knowledge, for example, photon statistics or flatness criteria.[16–22] Those methods are less sensitive to noise than filtered backprojection. However, they are more computationally expensive and some are very sensitive to a proper choice of parameters. A wavelet-approach was combined with linear interpolation to correct raw data corrupted by hip prosthesis, but with limited success.[32] To make use of the advantages of different methods, combinations of MAR algorithms have been published, for example, in Refs. 20, 23, and 24.

I.A.1. Frequency split

Frequency split approaches were applied in CT, for example, in Refs. 25–28 for other purposes than MAR. Different reconstruction algorithms were combined there in order to benefit from the advantages of the respective algorithms in different frequency bands.

The authors of Refs. 25 and 26 motivate a combination with reduced noise especially for spiral scans with very low pitch, were large amounts of redundant data are produced. Depending on the reconstruction algorithm, the level of cone-beam artifacts varies. The use of an exact reconstruction algorithm leads to cone-beam artifact-free images. However, this algorithm uses only certain parts of the raw data. In order to reduce noise and ensure a better dose-usage, images are reconstructed with an approximate algorithm, too. These images contain cone-beam artifacts, but cone-beam artifacts have relatively low frequencies. The low-frequency parts of a reconstruction using an exact algorithm can be combined with the high-frequency components of a reconstruction using an approximate one. In Ref. 27, the aim was to reconstruct high-resolution images with reduced cone-beam artifacts. The authors of Ref. 28 combined the reconstructions of an overview scan and a region-of-interest scan to reconstruct high-resolution images. A frequency split approach was already used in an algorithm for 3D PET reconstruction, which was proposed in Ref. 29.

II. METHODS

II.A. Idea

An uncorrected CT image of a patient with metal implants, reconstructed, for example, by filtered backprojection, contains artifacts, but it also still includes all information which is contained in the raw data. It is desirable that an MAR method preserves as much information from this
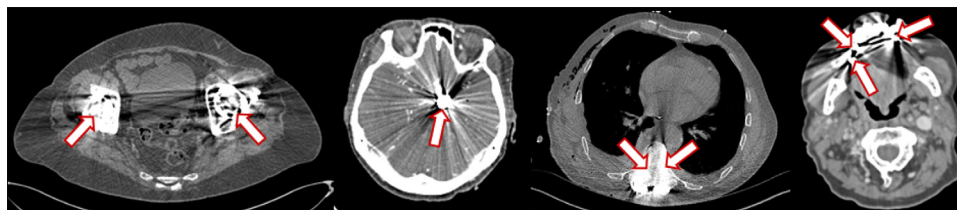

FIG. 1. Examples of CT images with metal artifacts. The arrows indicate the position of the metal implants. From left to right, a patient with bilateral hip prosthesis, one with neurocoil, with spine fixation, and with dental fillings is shown.
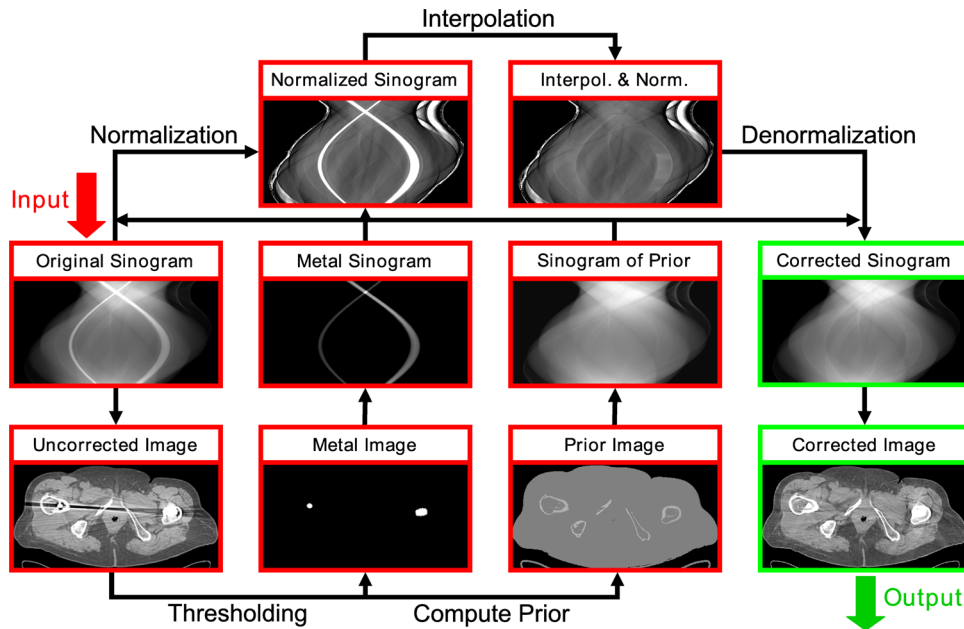
FIG. 2. Scheme of NMAR as described in Sec. II B 3. The original raw data are normalized before the replacement step by dividing each value of the original raw data by the corresponding value of the forward projection of a prior image.

image as possible while removing the artifacts. Choosing different window settings often reveals that close to metal implants, the outlines of anatomical structures are still detectable but have wrong CT values and are obscured by dark or bright artifacts. The idea of this work is based on the observation that in many cases, those parts of the metal artifacts which are caused by beam hardening and scatter have relatively low frequencies. High-pass filtering of the original image extracts the edge information, and therefore important anatomical detail, together with noise. The proposed algorithm, frequency split metal artifact reduction (FSMAR), reduces metal artifacts by combining the high frequencies of the uncorrected image, including the edge information close to implants, with the more reliable low frequencies of the image after correcting it with an inpainting-based MAR method. An example of a high-pass filtered CT image is included in the scheme in Fig. 3. While the edges of bones

close to the implants are visible in the high-pass filtered version, artifacts aside from noise show up only in a very moderate extent.

II.B. Algorithm

The FSMAR method consists of several steps: preprocessing, segmentation of metal, metal artifact reduction by an inpainting-based MAR method, frequency split, and spatial weighting. The different steps are explained in Subsections II B 1 to II B 4. A scheme of the algorithm can be found in Fig. 3.

II.B.1. Preprocessing

As a first step, an adaptive filter is applied to the raw data. For standard inpainting-based MAR approaches, this is not necessary, because the noisiest data, the data from the metal
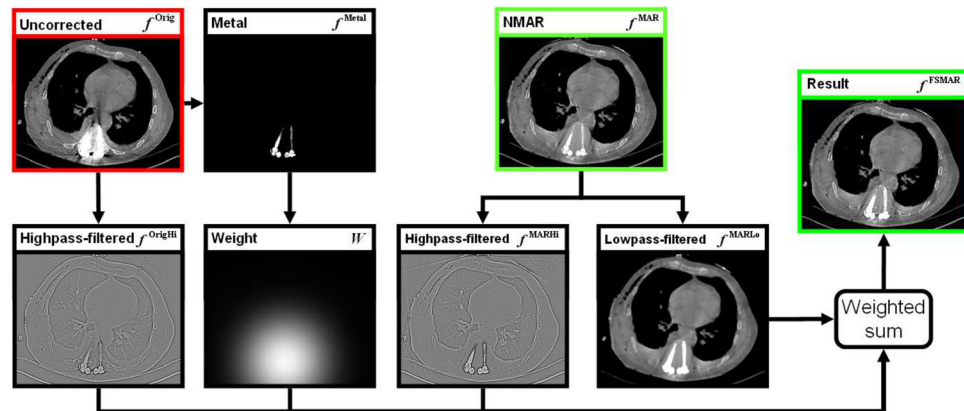

FIG. 3. The FSMAR-corrected image is a weighted sum of the high frequencies of the original image and the high and low frequencies of an image which was corrected by an inpainting-based MAR method. NMAR was used for the example images in this scheme. The weight is obtained by strongly smoothing the metal mask.
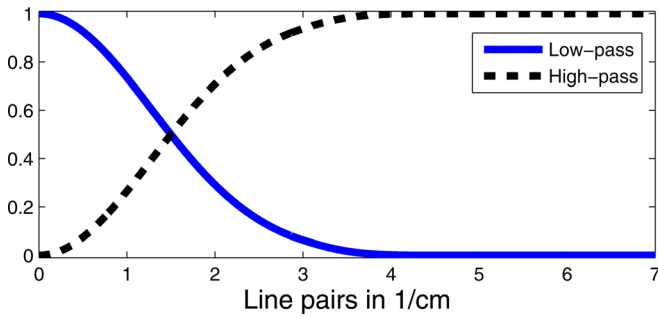
FIG. 4. Filter kernels for the frequency split.

shadow, are completely replaced. With FSMAR, data from the metal shadow are contributing to the final image and therefore, noise reduction is recommended. Details on adaptive filtering in the raw data domain can be found in Ref. 1. From the preprocessed raw data, an image f^{Orig} is reconstructed. All images in this work were reconstructed by filtered backprojection, but it is possible to combine FSMAR with other reconstruction algorithms, too.

II.B.2. Segmentation of metal

From the image f^{Orig}, a metal image f^{Metal} is segmented by simple thresholding. This image only contains the metal parts, all pixels which do not belong to the metal implants are set to zero. f^{Metal} is needed for the next step (metal artifact reduction by an inpainting-based MAR method) and the last step (spatial weighting). The threshold was chosen as a fixed percentage of the maximal CT value found in f^{Orig}. A minimum for the metal threshold of 3000 HU in the head and of 2000 HU in the rest of the body was chosen in order to avoid segmenting bone as metal.

II.B.3. Metal artifact reduction by an inpainting-based MAR method

In this step, an image corrected by an inpainting-based MAR method is computed. It is denoted as f^{MAR} here. First of all, the metal image f^{Metal} is forward projected. The location of the positive entries in this projection dataset defines the metal trace in the original raw data, which is the part that has to be replaced by an inpainting method. As mentioned in Sec. I, there are various different methods ranging from one dimensional interpolation to total variation-based inpainting, or methods using a forward projection. The method of choice in this work is normalized metal artifact reduction (NMAR) (normalized metal artifact reduction), details can be found in Ref. 13. For comparison, the frequency split method was also combined with an

MAR method without normalization. A standard approach as in Ref. 2 was chosen (here denoted as MAR1). For MAR1, the raw data from within the metal trace are replaced by linear interpolation in channel direction before the reconstruction. FSMAR can be combined with any MAR method that ensures the correction of the low-frequency parts of a CT image. All inpainting-based MAR methods are a possible choice as they completely replaces the raw data from the metal trace and therefore remove all metal artifacts. However, they often introduce new artifacts, as the complete information from the metal trace cannot be recovered. NMAR introduces less of those new artifacts, which was shown in Ref. 13. Moreover, first clinical evaluations of NMAR indicate significant improvements over other metal artifact reduction techniques, such that NMAR appears to be one of the first clinically relevant metal artifact reduction approaches.[33] A scheme of NMAR is provided in Fig. 2.

For this method, the original raw data are normalized with the forward projection of a prior image before the replacement step. These normalized projections are very homogeneous, and thus, linear interpolation yields more reliable results here. The prior image is obtained by first applying a simple inpainting-based MAR method, for example, MAR1. Second, after reconstruction, all pixel values below a threshold of, for example, −500 HU are identified as pixels in a air region and are set to −1000 HU. All pixels between −500 HU and a threshold for bone (depending on the body region) are set to 0 HU. Pixels above the bone threshold remain unchanged. Forward projection of the prior image yields the corresponding sinogram. Subsequently, the original sinogram is normalized by dividing it by the sinogram of the prior image pixel-wise. The nonzero entries in the metal projections determine where data in the normalized sinogram are replaced by interpolation. After the interpolation, the normalized sinogram is denormalized again by multiplying it with the sinogram of the prior image. This ensures that the traces of bones are properly connected through the metal trace. Reconstruction and reinsertion of the initial metal image yields the NMAR-corrected image.

Compared to other known MAR approaches, NMAR yields images with significantly less artifacts that result from interpolation errors.[13]

II.B.4. Frequency split

FSMAR combines parts of the high frequencies of the image f^{Orig} with image f^{MAR} (corrected with NMAR, MAR1, or some other inpainting-based MAR method). The low-pass filtered version of f^{MAR} is denoted as f^{MARLo} here. The high frequencies are denoted as f^{OrigHi} and f^{MARHi},

TABLE I. Overview of the scan parameters.

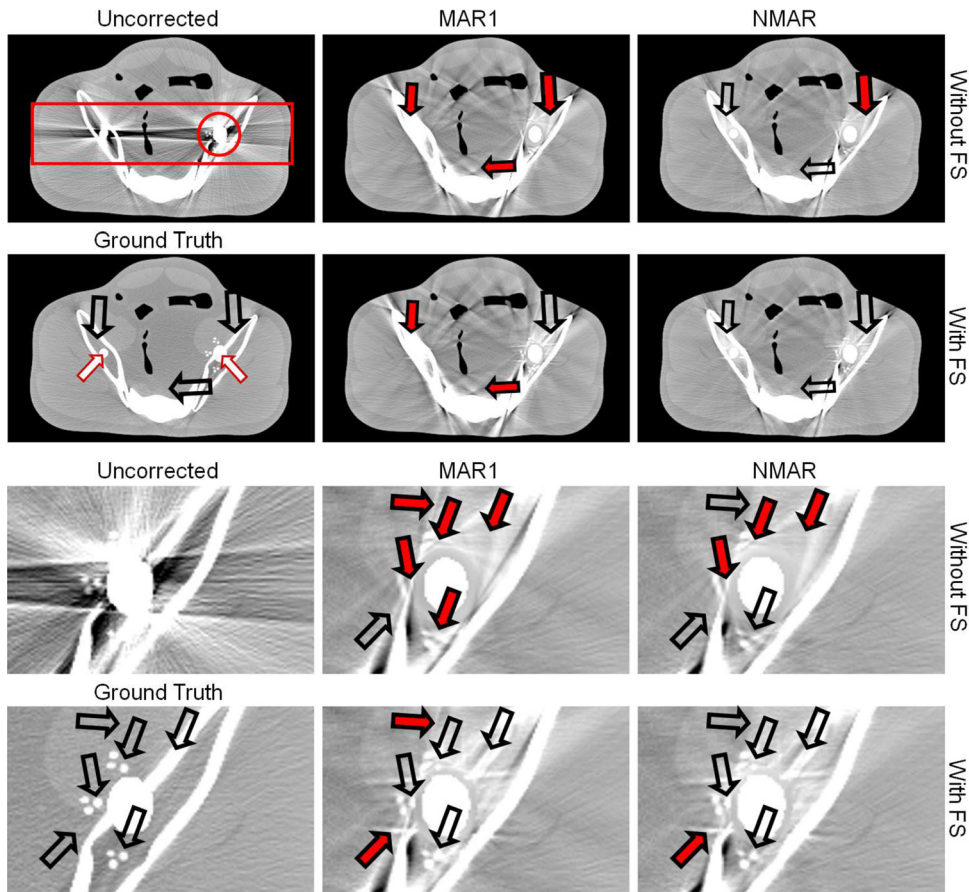|	Bilateral hip prosthesis	Unilateral hip prosthesis	Spine fixation	Dental fillings	Coil	Phantom
Tube voltage	120 (kV)	120 (kV)	120 (kV)	120 (kV)	80 (kV)	120 (kV)
Effective tube current	100 (mAs)	150 (mAs)	105 (mAs)	130 (mAs)	155 (mAs)	360 (mAs)
Spiral pitch value	0.6	0.6	0.7	0.8	0.7	0.7

FIG. 5. Simulation of the XCAT phantom with an additional bilateral hip prosthesis and nine small circular additional contrast details close to the right prosthesis. The prostheses are marked with the smaller arrows in the ground truth image. The two ROIs which are used in Table II are outlined in the uncorrected image. ROI 1 contains large parts of the phantom, while ROI 2 is restricted to the region around the right metal implant. While parts of the bone and the contrast details are blurred close to the right prosthesis in the NMAR and MAR1 images, the frequency split restores them ($C = 0$ HU/$W = 800$ HU).

respectivley. To obtain the high frequencies of an image, a low-pass filtered version of this image is subtracted

$$f^{\text{OrigHi}} = f^{\text{Orig}} - f^{\text{OrigLo}}, \quad f^{\text{MARHi}} = f^{\text{MAR}} - f^{\text{MARLo}}.$$

The low-pass filtered images are computed by a 2D-convolution with a Gaussian $G(\sigma)$

$$f^{\text{OrigLo}} = f^{\text{Orig}} * G(\sigma), \quad f^{\text{MARLo}} = f^{\text{MAR}} * G(\sigma).$$

As mentioned in Sec. II A, f^{MAR} is more reliable than f^{Orig} with respect to the low frequencies as it does not contain beam hardening and scatter artifacts due to metal anymore. f^{OrigHi} contains the edges and fine anatomical structures as well as some remaining streak artifacts due to noise. f^{MARHi} contains less noise, but close to the metal implants it also contains less edges of anatomical structures than f^{OrigHi}. Therefore, a spatially varying weight as described in Sec. II B 4 a is used to combine the advantages of both high-frequency images.

II.B.4.a. Spatial weighting. Using the complete high-frequency part of f^{Orig} would unnecessarily increase the noise in the whole corrected image. To avoid this, a weight is computed for each image pixel. For pixels close to metal implants, the weight is chosen higher than for pixels more distant to the implants. One way to obtain such a weight image W is to binarize the metal image, smooth it with a very strong low-pass filter and normalize it to a maximum value of one. An example of W

can be found in the scheme in Fig. 3. The final result, the FSMAR-corrected image f^{FSMAR} is the following weighted sum

$$f_{ij}^{\text{FSMAR}} = f_{ij}^{\text{MARLo}} + W_{ij}f_{ij}^{\text{OrigHi}} + (1 - W_{ij})f_{ij}^{\text{MARHi}},$$

$$\text{with } i = 1, \ldots, I, \ j = 1, \ldots, J,$$

where I is the number of rows and J the number of columns in an image.

II.B.4.b. Implementation. In our implementation, the convolution for the low-pass filtering was realized as a

TABLE II. Evaluation of FSMAR for the example of the XCAT phantom: RMSE of the different image versions f^{X} with f^{GT} as ground truth. The ROIs are marked in Fig. 5. The values are also given in percent, where the RMSE value of the uncorrected image is set to be 100% and used to normalize the other values. In both ROIs, the qualitative result comparing the different methods is the same: MAR1 is outperformed by FSMAR1 and NMAR is outperformed by FSNMAR. FSNMAR performs best with respect to this figure of merit.

		$f^{\text{Uncorrected}}$	f^{MAR1}	f^{FSMAR1}	f^{NMAR}	f^{FSNMAR}
ROI 1	RMSE(f^{X}, f^{GT})	159 HU	163 HU	153 HU	149 HU	131 HU
		100%	102%	96%	88%	82%
ROI 2	RMSE(f^{X}, f^{GT})	272 HU	277 HU	246 HU	265 HU	238 HU
		100%	102%	90%	97%	88%

Uncorrected   MAR1   NMAR
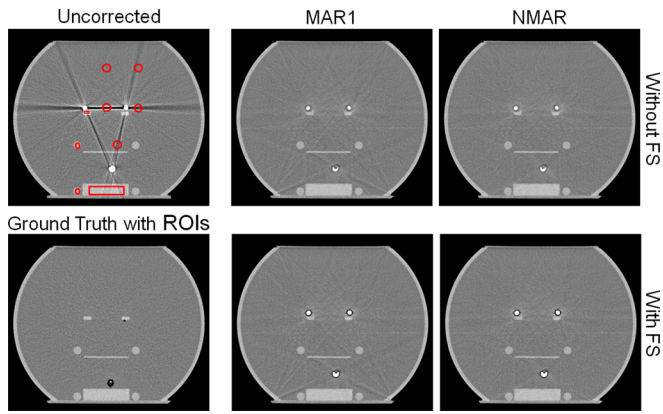
Ground Truth with ROIs

Without FS

With FS

FIG. 6. Scan of a spine phantom. For an objective evaluation, the mean CT value within ROIs containing only one material type was compared in the uncorrected image, in the corrected images and in the image of a slice without metal. The locations of the circular and rectangular ROIs are outlined in the uncorrected image. MAR1 reduced the RMSE to 67%, while both FSMAR1 and NMAR reduced it to 66%. FSNMAR reduced it to 65% ($C = 0$ HU$/W = 500$ HU).

multiplication in frequency domain. The filtering, and therefore the Fourier transform was applied in 2D for reasons of performance. Instead of applying a frequency split in the image domain, it is also possible to incorporate the high-pass and low-pass filter in the reconstruction kernel[27,28] and apply all filtering in raw data domain. Up to sampling and interpolation effects, this is equivalent.

II.B.4.c. Choice of parameters. Ideally, the algorithm would use a filter which separates edges of anatomical structures from the remainder of the image. With sophisticated nonlinear filters and heuristics of the spatial distribution of artifacts, it might be possible to separate artifacts and anatomical structures even better than with linear filtering. However, the goal of this work was to design a fast and robust algorithm without complicated parameter determination.

The same filtering parameters were used for all patients in this paper. A Gaussian with a full width at half maximum of three line pairs per cm (3/cm) was used as filter kernel. This corresponds to a standard deviation of $\sigma \approx 1.27$/cm. Figure 4 shows this low-pass filter and the corresponding high-pass filter in the frequency domain. The high-pass filter and the low-pass filter add up to one.

The choice of a suitable filter is independent of the reconstruction kernel which is used for the filtered backprojection. Different reconstruction kernels change which frequencies are emphasized, but they do not change the range of frequencies which an edge consists of. In Sec. IV C, results for different kernels are presented for comparison. As already mentioned, some components of the metal artifacts can lie in the frequency range of those edges which are brought back to the final image. By using the spatial weighting, this effect is limited to the

Uncorrected   MAR1   NMAR

Without FS
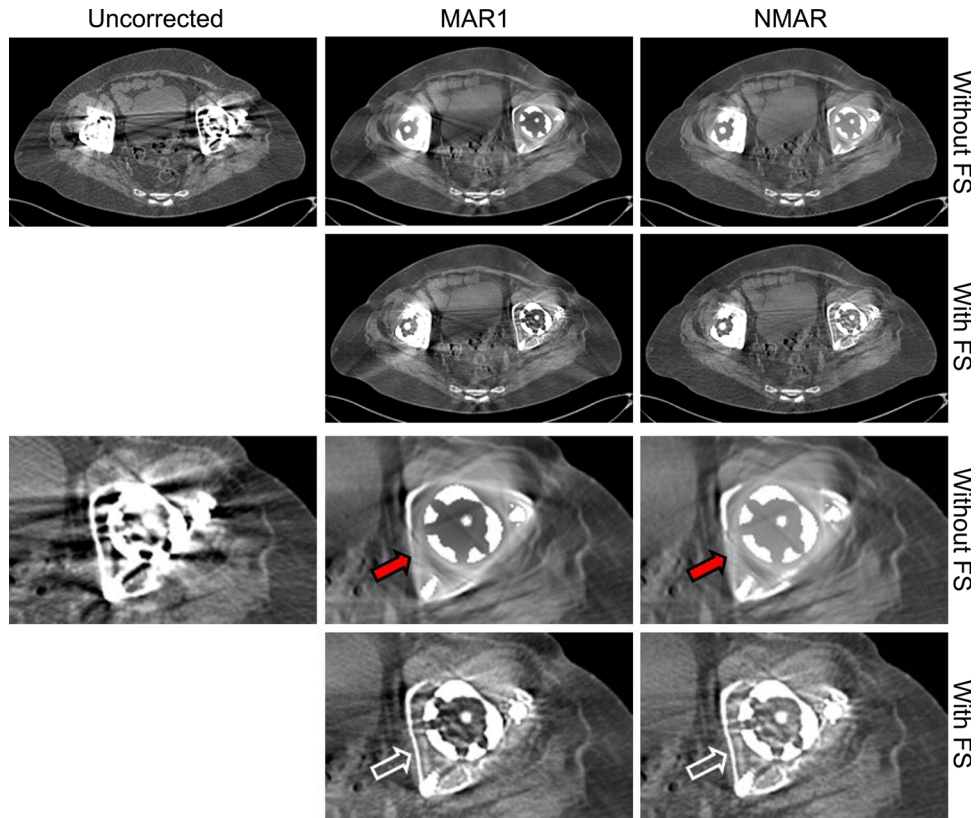
With FS

Without FS

With FS

FIG. 7. Patient with bilateral hip prosthesis. Solid arrows outlined in black are used in the magnified images to highlight the position where anatomical details are lost. Arrows outlined in white mark the same position in an image where the corresponding detail is visible, and thus imply that the used correction method is superior. The uncorrected image shows dark and bright artifacts. In the MAR1 result, those artifacts are removed, but between the two prostheses and tangent to the prosthesis, some new artifacts appear. The correction with NMAR is already quite satisfactory, but parts of the bone close to the implant are blurred or disappear. In the FSNMAR result, the bone is clearly visible and has a sharp contour everywhere ($C = 40$ HU$/W = 600$ HU).

vicinity of metal. The choice of the filter width is therefore always a compromise, and thus, there is by definition no ideal value for the width of the Gaussian. As results indicate, the slight remaining artifacts are of minor significance compared to the advantage of preserving important anatomical details.

III. SCAN AND RECONSTRUCTION DETAILS

A simulation and a phantom scan were used for quantitative evaluation. For the simulation, the XCAT phantom from Ref. 30 was used. Steel cylinders were added to the phantom to simulate a bilateral hip prosthesis. Additionally, nine small circular contrast details were added close to the right prosthesis. The simulated raw data were obtained using DRASIM (Siemens Healthcare, Forchheim, Germany). A circle scan was simulated with 100 kV tube voltage and a slice thickness of 0.6 mm. Noise and scatter was added to the raw data. The position of the slice was chosen to resemble the patient example in Fig. 8.

The phantom which was measured is a 30 cm acrylic fishbowl water phantom with metallic parts and nonmetallic parts to simulate a human spine with metal implants. The screws in the presented slice consist of surgical grade stainless steel and the nonmetallic parts aside from water are made from PMMA (polymethyl-methacrylat). The scan was acquired with a Siemens Somatom Definition Flash.

Additionally, five patient datasets from different Siemens scanners were used to evaluate FSMAR. The patients have different metal implants: total hip endoprostheses, dental fillings, a neurocoil, and an internal spine fixation. The patient with dental fillings and the patient with coil were scanned with the Siemens Somatom Definition Flash scanner. The patients with hip implants were scanned with a Siemens Somatom Definition AS+ and the patient with spine fixation with a Siemens Somatom Definition scanner. Table I gives an overview of the scan parameters.

All images in this paper were reconstructed using weighted filtered backprojection as in Ref. 31. The principle of frequency split metal artifact reduction, however, can be applied to images computed by a reconstruction algorithm of choice. The images were reconstructed on a 512×512 matrix with 0.6 mm slice thickness. For the patients with hip implants and the patient with coil, the images were reformatted after reconstruction to 1.5 mm slice thickness, for those patients with the dental fillings and the spine fixation to 1.0 mm slice thickness. A field of view of 300 mm was chosen for images of the head, 450 mm for images of other body regions.

IV. RESULTS

For comparison, the datasets were corrected with MAR1 and NMAR, and both with and without frequency split. Each figure contains the original image together with these four different corrected versions. As the threshold for metal is determined automatically from f^{Orig}, it has the same value for all image versions from one example. In this work, the focus is on the differences between the methods with and without frequency split,
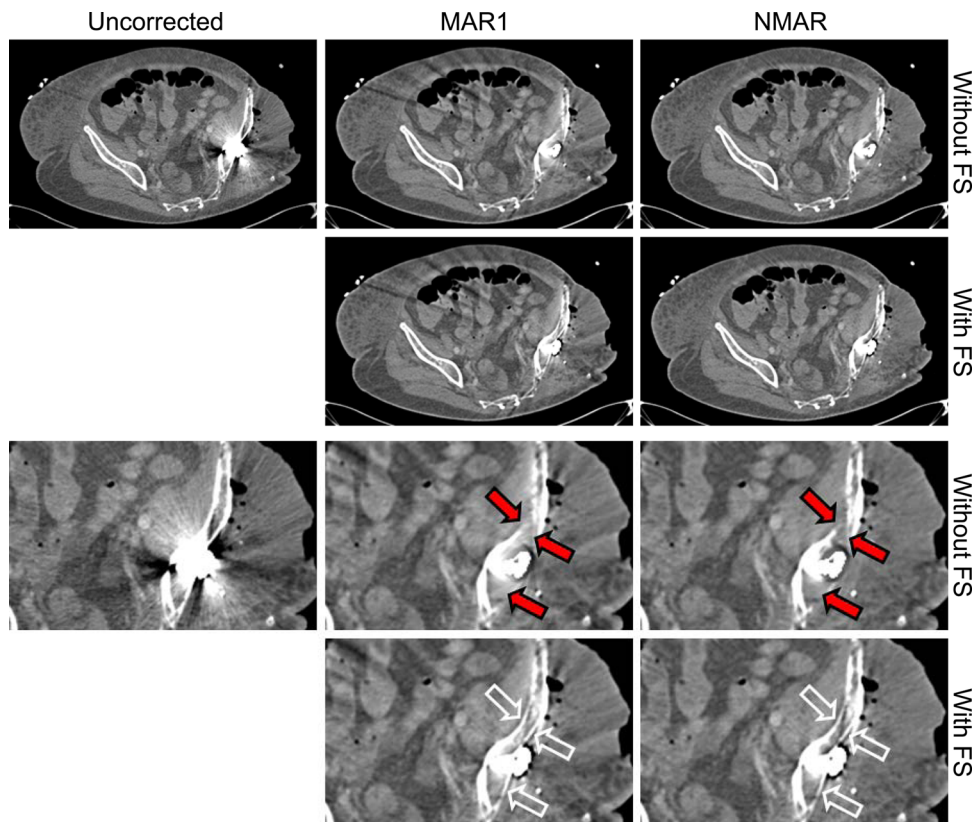

FIG. 8. Patient with unilateral hip endoprosthesis. Arrows as in Fig. 7. A cabel outside the patient also leads to a slight streak artifact. In the overview images, dark artifacts emerging from the metal and from the guts are visible in the MAR1 images with and without frequency split. Several of the thinner parts of the hip bone can only be seen in the images with frequency split. FSMAR with NMAR yields the best correction ($C = 40$ HU$/W = 600$ HU).

not between MAR1 and NMAR. The comparison of those methods has been addressed in Ref. 13 and it was shown that NMAR is superior to MAR1. However, the combination with MAR1 was included for reasons of completeness and because MAR1 is used in most papers on metal artifact reduction to compare other methods to a standard. A magnification of the vicinity of the implant is shown in each figure, too. For the patient results, solid arrows outlined in black are used in the magnified images to highlight the position where anatomical details are lost. Arrows outlined in white mark the same position in an image where the corresponding detail is visible, and thus imply that the used correction method is superior.

IV.A. Phantom results

A simulation of the XCAT phantom and the scan of a spine phantom were used to provide examples with ground truth and to evaluate FSMAR objectively.

IV.A.1. Phantom simulation

For the example of the XCAT phantom, the root mean square error (RMSE) was used as a figure of merit to compare different image versions objectively. When a ground truth image, denoted as f^{GT}, is given, the RMSE of an image f is

$$\mathrm{RMSE}(f, f^{GT}) = \sqrt{\frac{1}{I \cdot J} \sum_{i=1}^{I} \sum_{j=1}^{J} (f_{ij} - f_{ij}^{GT})^2},$$

where I is the number of rows and J the number of columns of the images f and f^{GT}.

The simulations were performed as described in Sec. III. A simulation of the phantom without metal serves as ground truth here. In the ground truth, the prosthesis was simulated as body tissue and not as metal in order to visualize the prosthesis but cause no metal artifacts.

The corrected images and the uncorrected image were compared with the ground truth by computing the RMSE within two ROIs: ROI 1 contains a large part of the phantom, while ROI 2 is restricted to the region close to the right prosthesis part, where metal artifacts severely degrade the image quality. The metal pixels were excluded from the computations. The images and the location of the ROIs are shown in Fig. 5. In Table II, the RMSE values are given. In ROI 2, the RSME
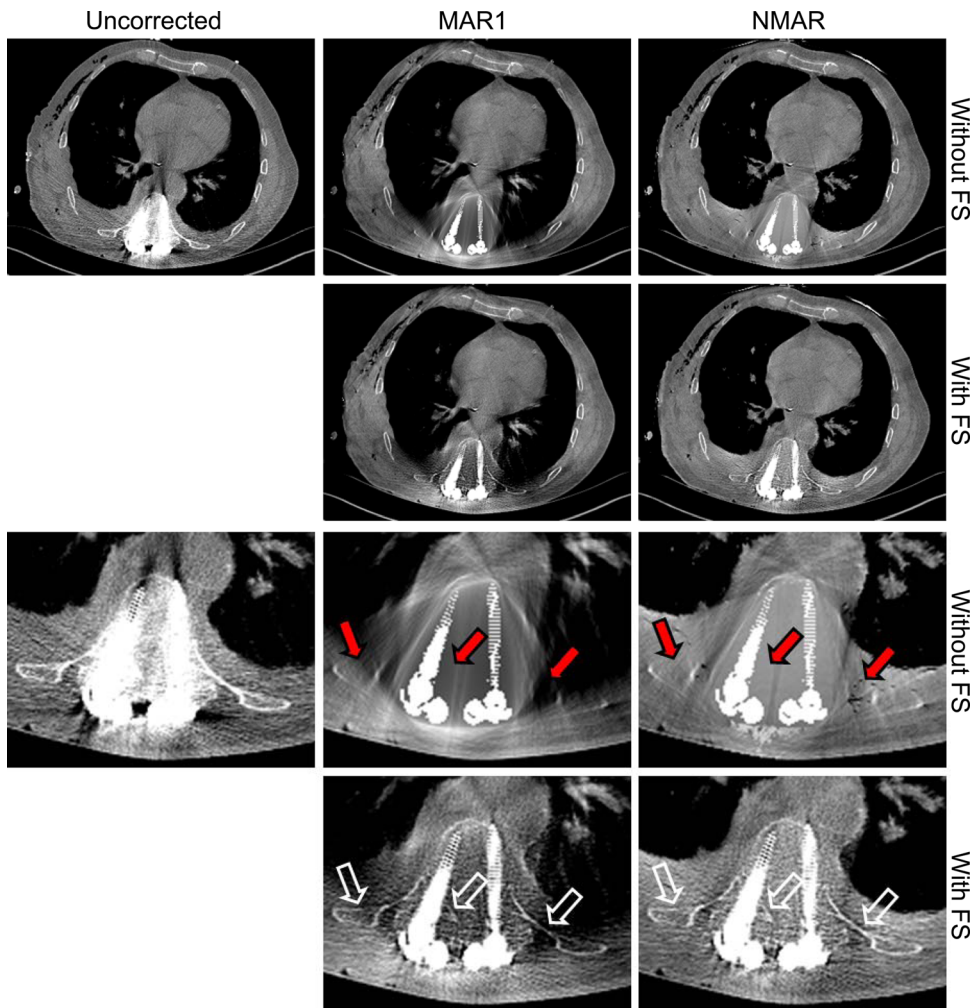

FIG. 9. Patient with internal spine fixation. Arrows as in Fig. 7. As large parts of raw data are replaced and the implants have not a round but an elongated shape, the MAR1 and the NMAR results are relatively blurry in the closest vicinity of the screws. With the frequency split, the outline of the vertebra can be recovered. Even between the screws, there are bone structures visible, which are obscured by artifacts in the original image ($C = 100$ HU/$W = 1000$ HU).

values in are higher than the respective values in ROI 1, as both metal artifacts and artifacts due to data replacement are stronger in ROI 2. The uncorrected image even performs better than the MAR1 image, indicating the high magnitude of the algorithm-induced artifacts. The combination of frequency split and MAR1 (FSMAR1), performs better than MAR1. NMAR outperforms MAR1 in both ROIs and outperforms FSMAR1 in ROI 1. The combination of NMAR with frequency split (FSNMAR) yields the lowest RMSE and therefore performs best with respect to this figure of merit. Similar to the patient example in Fig. 8, the bone close to the right implant is partly removed by MAR1 and NMAR. Also, the nine small circular contrast details, which were added to the phantom, are blurred by MAR1 and NMAR. In the FSMAR1 and FSNMAR results, the respective bone part is reconstructed. As the artifact between the two prosthesis parts in the original image has sharp edges, some slight steaks are visible in this area after FSMAR1 and FSNMAR. However, the contrast details are only visible clearly in the images using the frequency split.

IV.A.2. Phantom scan

For further quantitative evaluation of the reduction of artifacts, the mean CT values of different ROIs were com-

puted for the spine phantom. The ROIs were chosen manually and each ROI contains only pixels of one material type, either water or PMMA. The corrected images of a slice with metal and the uncorrected image were compared to the image of a slice without metal. Ten ROIs were evaluated for each version. The images which were compared are shown in Fig. 6. In the uncorrected image with metal, the root mean square error of the differences of the mean values within the different ROIs was 17 HU. This is relatively low, as some ROIs were distant to metal and the metal inserts are relatively small. MAR1 reduced the RMSE to 67% and FSMAR1 to 66%. NMAR reduced the RMSE to 66% and FSNMAR to 65%. FSNMAR therefore outperforms the other methods slightly. However, the advantage of the frequency split method is a better preservation of details. This can be appreciated more accurately when regarding the patient data with its fine bone structures.

IV.B. Patient results

IV.B.1. Hip prosthesis

The first patient has a bilateral hip prosthesis. The results are shown in Fig. 7. The uncorrected image shows dark and bright artifacts especially between the two parts of the
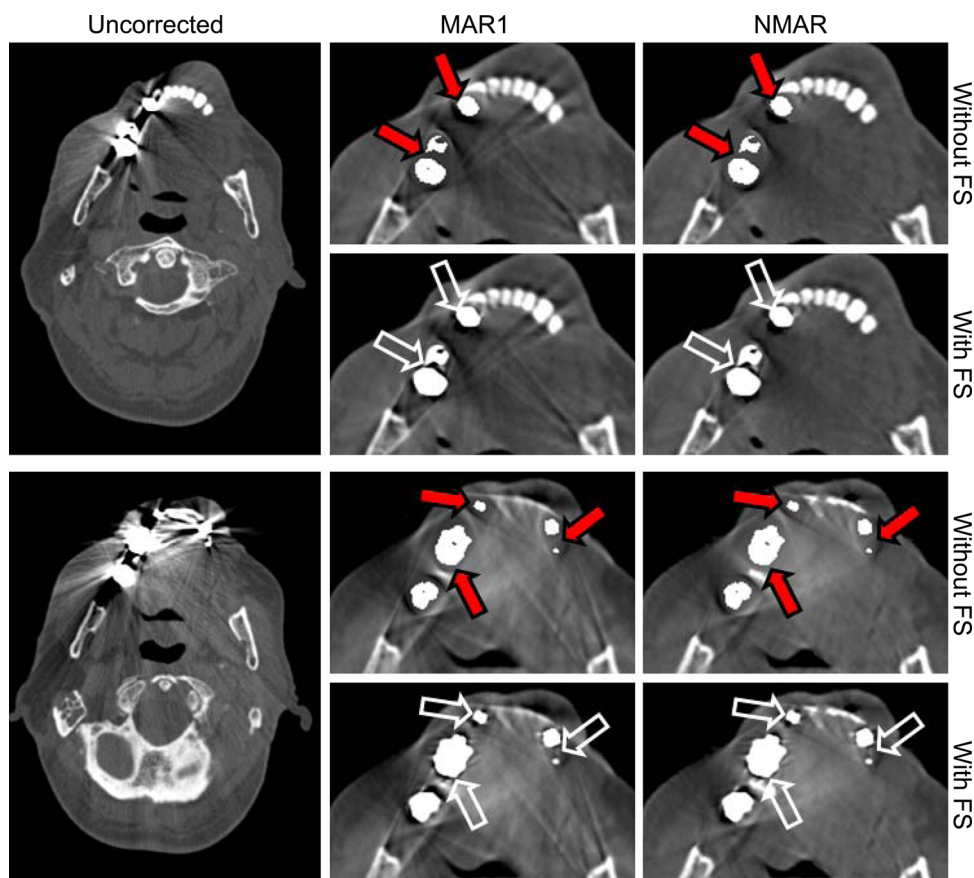

FIG. 10. Patient with dental fillings. Arrows as in Fig. 7. In the MAR1 and NMAR images without frequency split, the reinserted metal implants are too small. Additionally, the edges appear artificially sharp. Using the frequency split method, the true outlines of the smaller implants are restored as the outline does not depend on the metal threshold here. However, this is an example where some details are removed by all MAR methods. Also, some parts of the artifacts are sharp enough here to be reintroduced by the frequency split ($C = 400$ HU$/W = 2000$ HU).

prosthesis. In the MAR1 result, those artifacts are removed, but between the two prostheses and tangent to the prostheses, some new artifacts appear. The correction with NMAR without frequency split is already quite satisfactory, but part of the bone close to the implant is heavily blurred. In the results with frequency split, the bone is clearly visible and has a sharp contour everywhere. The FSNMAR result is superior to the FSMAR1 result as artifacts from the MAR1 image are visible in the FSMAR1 image, too.

In Fig. 8, the results for a second patient with hip prosthesis are presented. This patient has a unilateral prosthesis, the slice shown in this example is in a higher position than in the other example. Although the cross-section of the implant is relatively small in this slice, several of the thinner parts of the hip bone can be only seen in the images with frequency split. This is marked by arrows in the magnified images. From certain view directions in the raw data domain, these fine structures are completely within the metal shadow. In the overview images, dark artifacts emerging from the metal and

from the guts are visible in the MAR1 and FSMAR1 images. Therefore, the FSNMAR image is the best result in this case.

IV.B.2. Spine fixation

The results for the third patient, the example with an internal spine fixation, are shown in Fig. 9. The artifacts are mostly in the direction parallel to the screws. This dataset is an example where data from within the metal trace still contain a lot of information. The intersection lengths of rays with metal are relatively short in most views in this example, especially in the lateral direction. However, in those directions, a significant part of the data is replaced and therefore disregarded by inpainting-based MAR methods. Therefore, the MAR1 and NMAR results are relatively blurry in the closest vicinity of the screws. By FSMAR, the vertebra can be recovered. Between the screws, there are now even bone structures visible which are obscured by artifacts in the original image. This demonstrates that FSMAR can even restore
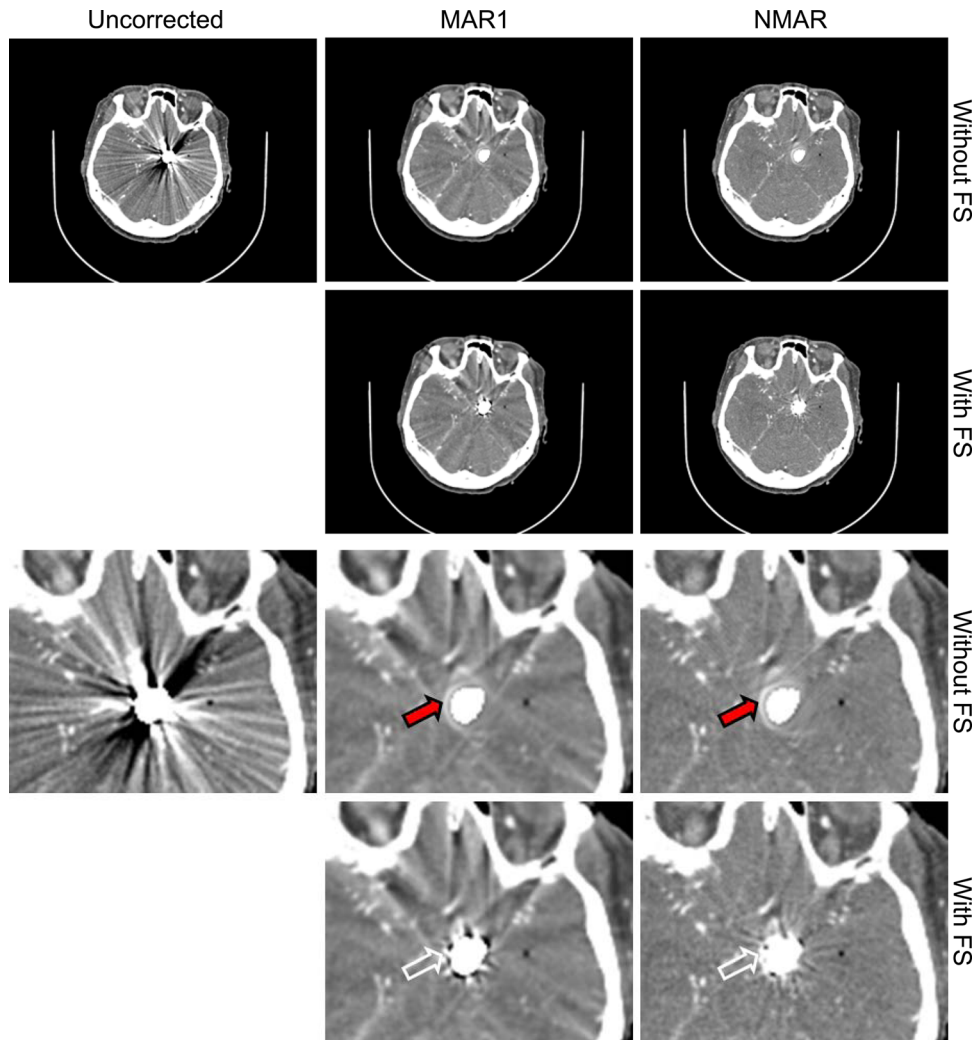

FIG. 11. Patient after coiling of an intracranial aneurysm. Arrows as in Fig. 7. The uncorrected image exhibits strong dark and bright streak artifacts, which make the region around the coil almost useless. The artifacts are removed by both MAR1 and NMAR, even if MAR1 introduces new artifacts. Close to the coil, a white ring-shaped artifact and slight blurring are visible after MAR1 and NMAR. In the frequency split versions, some slight streaks are reintroduced, but the blurring is removed ($C = 40$ HU/$W = 600$ HU).

structures between or within metal implants. This cannot be achieved with pure inpainting-based MAR methods, because all the data contributing to this image region are replaced completely. No parts of the raw data outside the metal trace, which are used to inpaint the metal trace, contain information about this region. The FSNMAR result is again superior to the FSMAR1 result as the NMAR image is more reliable than the MAR1 image.

IV.B.3. Dental fillings

The results for a patient with dental fillings are shown in Fig. 10. As mentioned in the introduction, dental fillings are often very dense. When a patient has several dental fillings as in this case, the bright and dark artifacts can make parts of the jaw region diagnostically useless. With such dense implants, the assumption that the raw data from within the metal trace contain no valuable information anymore is more reasonable than for the examples above. Also, parts of the artifacts are often sharp enough to be reintroduced by the frequency split.

On the other hand there is an advantage of using FSMAR for dental fillings, too. Thresholds for dental implants have to be relatively high (for this patient about 4000 HU compared to about 2500 HU for the hip prostheses). If the metal threshold

is chosen too low, artifacts are segmented as metal, too, leading to unnecessarily large amounts of data being replaced. As mentioned in Sec. II B 2, the thresholds for the segmentation of metal are determined automatically. In this example, the threshold is relatively high. The consequence is that some of the segmented metal implants, which are reinserted after the correction, are slightly too small. Additionally, the edges of the implants appear artificially sharp. This can be seen in Fig. 10 in the MAR1 and NMAR images without frequency split. Using the frequency split method, the outlines of the implants are restored.

IV.B.4. Coiling

The last example is a patient after coiling of an intracranial aneurysm. The results are shown in Fig. 11. The uncorrected image exhibits strong dark and bright streak artifacts, which make the region around the coil almost useless. A bleeding close to the coil would be very hard to detect in this case. The artifacts are removed by both MAR1 and NMAR, even if MAR1 introduces new artifacts. Close to the coil, a white ring-shaped artifact and slight blurring are visible after MAR1 and NMAR. In the frequency split versions, some slight streaks close to the coil are reintroduced here, but the blurring is removed.
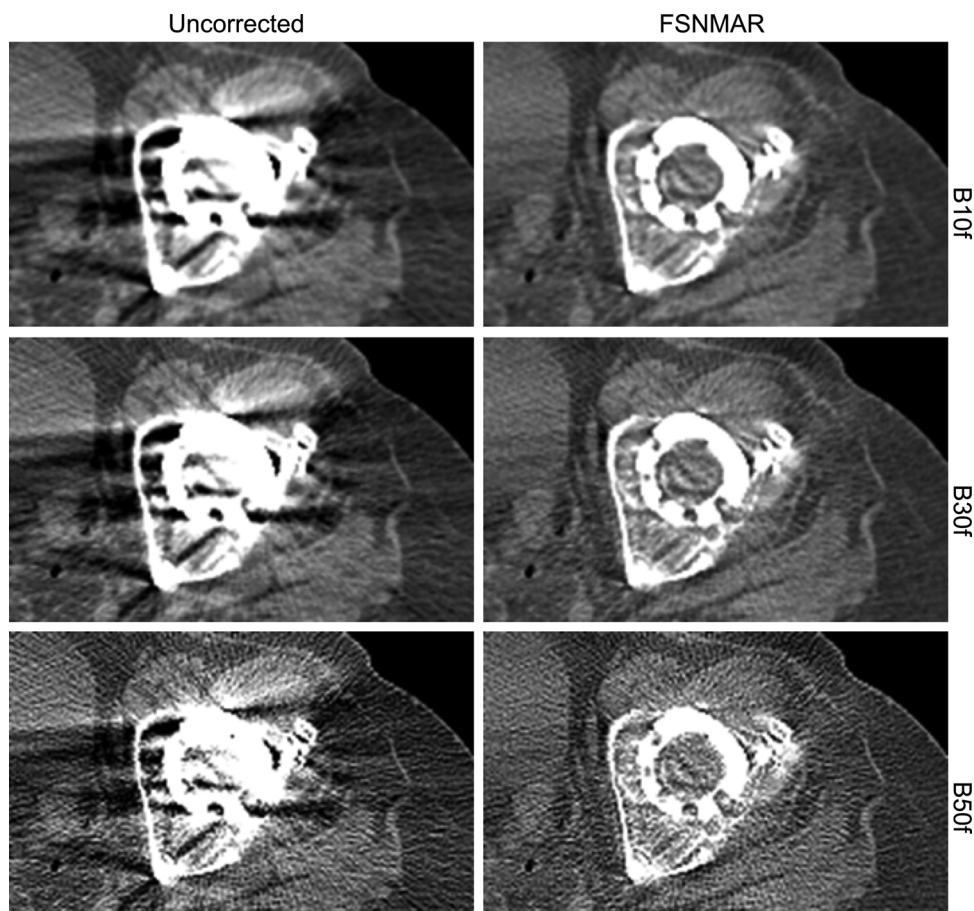

FIG. 12. Patient with bilateral hip prosthesis, reconstructed with different reconstruction kernels (Siemens kernels B10f, B30f, and B50f). The preservation of bone close to the implants is independent of the choice of the kernel ($C = 40$ HU$/W = 600$ HU).

IV.C. Different reconstruction kernels

FSNMAR was also tested with different reconstruction kernels. Figure 12 shows the results for the patient with bilateral hip prosthesis, reconstructed with three kernels of different sharpness (Siemens kernels B10f, B30f, and B50f, with B10f being the softest one, B meaning body-kernel). For each kernel, the uncorrected and the FSNMAR-corrected image are shown. Except for the reconstruction kernel, exactly the same parameters were used in all cases. Both the uncorrected and the corrected images are noisier for the sharper kernels, of course. The preservation of bone close to the implants is independent of the choice of the kernel.

V. DISCUSSION

FSMAR is based on the assumption that data from the metal trace still contain usable information. In some of the cases, especially for metals of moderate density like titanium, a physical correction can be an alternative. However, a physical correction of beam hardening or even scatter artifacts due to metal is computationally and algorithmically much more demanding. Also, no general procedure for different types of implants was yet found which is robust and tested for various different cases. To finally prove the success of FSNMAR, a more objective and extensive clinical evaluation by medical experts is needed. However, the algorithm yields very promising results and it is fast and robust enough for an application in clinical routine.

VI. SUMMARY AND CONCLUSIONS

A conceptually new algorithm for MAR has been introduced and successfully applied to several patient datasets. The proposed algorithm, FSMAR, combines parts of the high frequencies of an original image with an image that was corrected by an inpainting-based MAR algorithm. In images corrected with a pure inpainting-based MAR method, the region around a metal implant is often blurred. This is because these methods completely replace those parts of the raw data which are affected by metal. The idea of FSMAR is based first on the observation that those parts of the metal artifacts which are caused by beam hardening and scatter have relatively low frequencies. Second, images with metal implants often still contain anatomical structures close to metal implants. Those structures are obscured by artifacts, but their edges can be extracted by high-pass filtering.

FSMAR has several advantages compared to other MAR methods. In the corrected images, clear edges and fine anatomical details are recovered. As demonstrated, FSMAR can even restore structures between or within metal implants under the condition that they are sharp enough. The images exhibit a natural noise structure and no artificial image impression is created. The outline of metal implants is more accurate than after applying MAR methods that use segmentation by simple thresholding of metal but do not use edge information. In addition to a correction with an inpainting-based MAR method, FSMAR requires only the image-based filtering, multiplication, and addition of three volumes.

Thus, compared to iterative methods or methods with complex inpainting schemes, the algorithm is computationally very efficient.

A quantitative evaluation was performed using two examples: a simulation of the XCAT phantom and a scan of a spine phantom. Metal-free images as ground truth were compared to images corrected with MAR methods with and without frequency split by computing the root mean square error in several ROIs. The suitability of FSMAR to reduce metal artifacts was confirmed, especially for the combination with NMAR. The proposed algorithm was applied to datasets with different types of metal implants. For small implants with a circular cross-section, as for example, coils or dental fillings, FSMAR does not create an unnatural appearance due to blurring in contrast to pure inpainting-based MAR methods. Additionally, the outlines of the metal implants are more reliable. If the metal implants have a more irregular shape or a larger cross-section, the benefit of FSMAR compared to methods without frequency split is even higher. The algorithm yields sharper images with significantly more details close to the metal implants.

It was found that FSMAR should be used together with NMAR. This combination ensures the reduction of metal artifacts and delivers results with high image quality even close to metal implants.

Summarizing, we showed that adding the frequency split to existing metal artifact reduction approaches improves the visibility of small details such as bone segments. Combining frequency split with the normalized metal artifact reduction algorithm yields FSNMAR, a computationally efficient and very successful approach which appears to be suitable to be used in clinical routine.

[a]Author to whom correspondence should be addressed. Electronic mail: marc.kachelriess@dkfz.de.

[1]M. Kachelrieß, O. Watzke, and W. A. Kalender, "Generalized multidimensional adaptive filtering (MAF) for conventional and spiral single-slice, multi-slice, and cone-beam CT," Med. Phys. **28**(4), 475–490 (2001).

[2]W. A. Kalender, R. Hebel, and J. Ebersberger, "Reduction of CT artifacts caused by metallic implants," Radiology **164**(2), 576–577 (1987).

[3]A. H. Mahnken, R. Raupach, J. E. Wildberger, B. Jung, N. Heussen, T. G. Flohr, R. W. Günther, and S. Schaller, "A new algorithm for metal artifact reduction in computed tomography: In vitro and in vivo evaluation after total hip replacement," Invest. Radiol. **38**(12), 769–775 (2003).

[4]B. Kratz and T. M. Buzug, "Metal artifact reduction in computed tomography using nonequispaced Fourier transform," *Nuclear Science Symposium Conference Record (NSS/MIC)*, (IEEE, Orlando, Florida, 2009), pp. 2720–2723.

[5]K. Y. Jeong and J. B. Ra, "Reduction of artifacts due to multiple metallic objects in computed tomography," *Medical Imaging 2009: Physics of Medical Imaging*, Vol. 7258, No. 1, p. 72583E (2009).

[6]L. Yu, H. Li, J. Mueller, J. Kofler, X. Liu, A. Primak, J. Fletcher, L. Guimaraes, T. Macedo, and C. McCollough, "Metal artifact reduction from reformatted projections for hip prostheses in multislice helical computed tomography: Techniques and initial clinical results," Invest. Radiol. **44**(11), 691–696 (2009).

[7]W. J. H. Veldkamp, R. M. S. Joemai, A. J. van der Molen, and J. Geleijns, "Development and validation of segmentation and interpolation techniques in sinograms for metal artifact suppression in CT," Med. Phys. **37**(2), 620–628 (2010).

[8]B. Kratz, S. Ens, J. Müller, and T. M. Buzug, "Reference-free ground truth metric for metal artifact evaluation in CT images," Med. Phys. **38**(7), 4321–4328 (2011).

[9]J. Wei, L. Chen, G. A. Sandison, Y. Liang, and L. X. Xu, "X-ray CT high-density artefact suppression in the presence of bones," Phys. Med. Biol. **49**(24), 5407–5418 (2004).

[10]M. Bal and L. Spies, "Metal artifact reduction in CT using tissue-class modeling and adaptive prefiltering," Med. Phys. **33**(8), 2852–2859 (2006).

[11]J. Müller and T. M. Buzug, "Spurious structures created by interpolation-based CT metal artifact reduction," Proc. SPIE. **7258**(1), 1Y1–1Y8 (2009).

[12]E. Meyer, F. Bergner, R. Raupach, T. Flohr, and M. Kachelrieß, "Normalized metal artifact reduction (NMAR)in computed tomography," Nuclear Science Symposium Conference Record (NSS/MIC), (IEEE, Orlando, Florida, 2009), pp. 3251–3255.

[13]E. Meyer, R. Raupach, M. Lell, B. Schmidt, and M. Kachelrieß, "Normalized metal artifact reduction (NMAR) in computed tomography," Med. Phys. **37**(10), 5482–5493 (2010).

[14]D. Prell, Y. Kyriakou, T. Struffert, A. Dörfler, and W. Kalender, "Metal artifact reduction for clipping and coiling in interventional C-arm CT," Am. J. Neuroradiol. **31**(4), 634–639 (2010).

[15]F. Boas and D. Fleischmann, "Evaluation of two iterative techniques for reducing metal artifacts in computed tomography," Radiology **259**(3), 894–902 (2011).

[16]G. Wang, D. L. Snyder, J. A. O'Sullivan, and M. W. Vannier, "Iterative deblurring for CT metal artifact reduction," IEEE Trans. Med. Imaging **15**(5), 657–664 (1996).

[17]B. De Man, J. Nuyts, P. Dupont, G. Marchal, and P. Suetens, "An iterative maximum-likelihood polychromatic algorithm for CT," IEEE Trans. Med. Imaging **20**(10), 999–1008 (2001).

[18]M. Oehler and T. M. Buzug, "Modified MLEM algorithm for artifact suppression in CT," Nuclear Science Symposium Conference Record, (IEEE, San Diego, California, 2006), Vol. 6, pp. 3511–3518.

[19]C. Lemmens, D. Faul, J. Hamill, S. Stroobants, and J. Nuyts, "Suppression of metal streak artifacts in CT using a MAP reconstruction procedure,"

Nuclear Science Symposium Conference Record, (IEEE, San Diego, California, 2006), Vol. 6, pp. 3431–3437.

[20]C. Lemmens, D. Faul, and J. Nuyts, "Suppression of metal artifacts in CT using a reconstruction procedure that combines MAP and projection completion," IEEE Trans. Med. Imaging **28**(2), 250–260 (2009).

[21]L. Ritschl, F. Bergner, C. Fleischmann, and M. Kachelrieß, "Improved total variation-based CT image reconstruction applied to clinical data," Phys. Med. Biol. **56**(6), 1545–1561 (2011).

[22]X. Zhang, J. Wang, and L. Xing, "Metal artifact reduction in x-ray computed tomography (CT) by constrained optimization," Med. Phys. **38**(2), 701–711 (2011).

[23]O. Watzke and W. A. Kalender, "A pragmatic approach to metal artifact reduction in CT: merging of metal artifact reduced images," Eur. Radiol. **14**(5), 849–856 (2004).

[24]H. Li, L. Yu, X. Liu, J. G. Fletcher, and C. H. McCollough, "Metal artifact suppression from reformatted projections in multislice helical CT using dual-front active contours," Med. Phys. **37**(10), 5155–5164 (2010).

[25]H. Kudo, F. Noo, M. Defrise, and T. Rodet, "New approximate filtered backprojection algorithm for helical cone-beam CT with redundant data," Nuclear Science Symposium Conference Record, (IEEE, Portland, Oregon, 2003), Vol. 5, pp. 3211–3215.

[26]H. Kudo, T. Rodet, F. Noo, and M. Defrise, "Exact and approximate algorithms for helical cone-beam CT," Phys. Med. Biol. **49**(13), 2913–2931 (2004).

[27]G. Shechter, T. Koehler, A. Altman, and R. Proksa, "The frequency split method for helical cone-beam reconstruction," Med. Phys. **31**(8), 2230–2236 (2004).

[28]C. Maaß, M. Knaup, and M. Kachelrieß, "New approaches to region of interest computed tomography," Med. Phys. **38**(6), 2868–2878 (2011).

[29]E. Tanaka, S. Mori, K. Shimizut, E. Yosikawa, T. Yamashita, and H. Murayama, "Moving slice septa and pseudo three-dimensional reconstruction for multi-ring PET," Phys. Med. Biol. **37**(3), 661–672 (1992).

[30]W. Segars and B. Tsui, "The MCAT, NCAT, XCAT and MOBY phantoms," Handbook of Anatomical Models for Radiation Dosimetry, X.G. Xu and K. F. Eckerman, (Informa Healthcare USA, New York, NY, 2010), pp. 105–134.

[31]K. Stierstorfer, A. Rauscher, J. Boese, H. Bruder, S. Schaller, and T. Flohr, "Weighted FBP—A simple approximate 3D FBP algorithm for multislice spiral CT with good dose-usage for arbitrary pitch," Phys. Med. Biol. **49**(11), 2209–2218 (2004).

[32]S. Zhao, D. D. Robertson, G. Wang, B. Whiting, and K. T. Bae, "X-Ray CT metal artifact reduction using wavelets: an application for imaging total hip prostheses," TMI. **19**(2), 1238–1247 (2000).

[33]M. Lell, E. Meyer, M. Kuefner, M. May, R. Raupach, M. Under, and M. Kachelrieß, "Normalized metal artifact reduction in head and neck computed tomography," Inv. Rad. (in press).